CHIN. PHYS. LETT. Vol. 36, No. 9 (2019) 094201

A Photon-Counting Full-Waveform Lidar *

Bing-Cheng Du(杜秉乘)[1], Zhao-Hui Li(李召辉)[1], Guang-Yue Shen(申光跃)[1], Tian-Xiang Zheng(郑天翔)[1], Hai-Yan Zhang(张海燕)[1], Lei Yang(杨雷)[1], Guang Wu(吴光)[1,2]**

[1]*State Key Laboratory of Precision Spectroscopy, East China Normal University, Shanghai 200062*
[2]*Collaborative Innovation Center of Extreme Optics, Shanxi University, Taiyuan 030006*

(Received 18 May 2019)

We present the results of using a photon-counting full-waveform lidar to obtain detailed target information with high accuracy. The parameters of the waveforms (i.e., vertical structure, peak position, peak amplitude, peak width and backscatter cross section) are derived with a high resolution limit of 31 mm to establish the vertical structure and scattering properties of targets, which contribute to the recognition and classification of various scatterers. The photon-counting full-waveform lidar has higher resolution than linear-mode full-waveform lidar, and it can obtain more specific target information compared to photon-counting discrete-point lidar, which can provide a potential alternative technique for tomographic surveying and mapping.

PACS: 42.68.Wt, 42.79.Pw, 85.60.Gz DOI: 10.1088/0256-307X/36/9/094201

Lidar (light detection and ranging) is one of the most accurate remote sensing techniques and it is considered to hold a large potential in various applications, such as topography, three-dimensional (3D) city modeling, power line detection, forest structure measurements and carbon mapping.[1–4] However, most of the time-of-flight lidars only provide 3D coordinates of the targets with discrete echo points. So far, a full-waveform lidar has been proposed that records the entire backscattering echo waveforms of the targets for the classification of the targets.[5–12] A full-waveform lidar traditionally uses a wide-band linear optical detector and a high-speed analog-to-digital converter to obtain the waveform of the echo light. This requires a higher power pulsed laser than that of a typical lidar. In a linear-mode lidar geoscience laser altimeter system (GLAS), the photon number at the receiving end was measured at a rate of more than 10000 photons per pulse.[13] Nonetheless, single-photon detectors have been widely used to promote the performance of lidars.[14–19] A photon-counting lidar transmits shorter pulses and detects the scattered light at levels as low as a single photon, which contributes to a low-power consumption and high-precision measurements with the time-correlated single-photon counting (TCSPC) technique.[20–34]

In this Letter, we demonstrate a photon-counting full-waveform lidar. A pulsed laser with a high repetition rate of 2 MHz is used to count photon pulses. These photon counts build an echo waveform that can be reconstructed with the TCSPC technique. The complexity of the waveforms is greatly reduced with short laser pulses, which facilitates the extraction of the signal pulse information. By virtue of the echo full-waveforms, more parameters of the scattering surface can be analyzed than in a traditional discrete-point lidar, such as the vertical structure, peak position, peak amplitude, peak width and backscatter cross section, which are utilized to characterize the surface features of the targets for classification.

The experimental setup is shown in Fig. 1(a). In the experiment, a laser diode was directly driven by an electric pulse to generate short laser pulses at 1550 nm with a pulse duration of ∼185 ps. The laser was amplified by an erbium-doped fiber amplifier (EDFA) with an energy of ∼2.0 nJ per pulse at the output of a fiber collimator (Col). The laser beam was 4.0 mm in diameter with a divergence angle of ∼0.35 mrad. The transmitted laser beam was coaxial with a Newtonian receiving telescope in diameter of 120 mm and focal length of 650 mm. The echo photons from the targets were collected by the telescope and coupled into a fiber-pigtailed single-photon detector (SPD) with a fiber core of 62.5 μm in diameter. The single-photon detector was an InGaAs/InP avalanche photodiode (APD) that was cooled at 240 K. It was operated in a quasi-continuous Geiger mode with sinusoidal waves gating at 1 GHz. The detection efficiency was 3.58% for nonsynchronous photons, and the dark count rate was 2.0×10^4 cps (counts per second). The output of the SPD was connected to the 'Stop' of the TCSPC (PicoHarp400), while the synchronous trigger signal of the DFB laser diode was connected to the 'Start' of the TCSPC. The time interval between the Start and the Stop signals indicated the flight time of the photons. The overall time resolution (i.e., the full width at half maximum (FWHM)) of the system was approximately 208 ps, including the duration of the laser pulse (185 ps), the time jitter of the SPD (90 ps), and the temporal resolution of the TCSPC (32 ps).

*Supported by the National Natural Science Foundation of China under Grant Nos 11774095, 11804099 and 11621404, the Shanghai Basic Research Project under Grant No 18JC1412200, and the Program of Introducing Talents of Discipline to Universities under Grant No B12024.

**Corresponding author. Email: gwu@phy.ecnu.edu.cn

© 2019 Chinese Physical Society and IOP Publishing Ltd

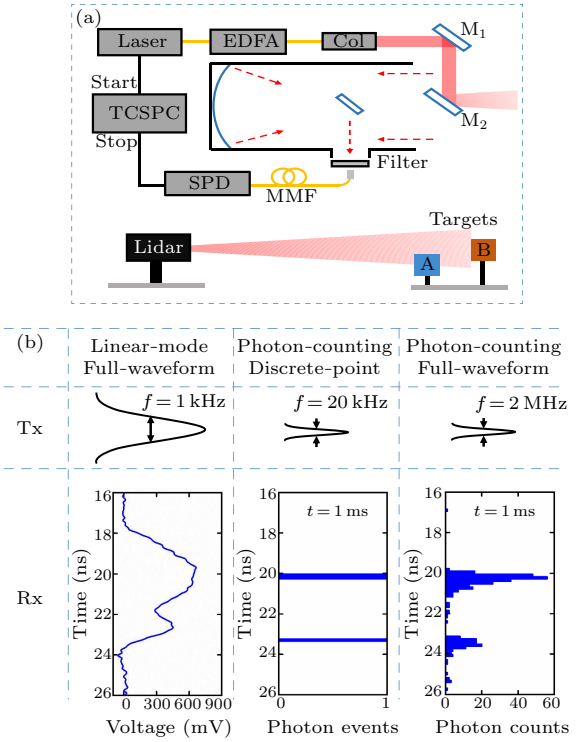

Fig. 1. (a) Experimental setup of the photon-counting lidar system based on the SPD. The components of our setup included: an erbium-doped fiber amplifier (EDFA), collimator (Col), high-reflection mirrors (M_1, M_2), an optical short bandpass filter, a multimode fiber (MMF), and two boxes with different colors (A, B). (b) A schematic diagram of different types of lidar systems. Tx is the transmitted laser pulse, and Rx is the return waveform. The photon-counting lidar transmits shorter and lower-energy laser pulses than the linear-mode systems. The conventional discrete-point photon-counting lidar obtains only discrete positional information, whereas the photon-counting full-waveform lidar records sharper waveforms with higher resolution than the linear-mode lidar.

Figure 1(b) demonstrates the results of the lidar operated in three modes. The targets are two boxes separated by 50 cm. In the linear-mode full-waveform lidar, an InGaAs pin diode with a bandwidth of 300 MHz is used, and the output is sampled by a 3.5 GHz-bandwidth digital oscilloscope. Owing to the low sensitivity of the linear optical detector, the duration of the laser pulse is 3 ns to generate high energy laser pulses. The photon-counting lidar, in contrast, transmits a shorter pulsed laser (∼185 ps) with lower energy. The echo counting rate for photon counting lidar is 0.15 per pulse. In the photon-counting discrete-point lidar, only discrete photon events are recorded during short measurement periods of 1 ms, which is the same technique used for the airborne lidar, slope imaging multi-polarization photon-counting lidar (SIMPL) and the spaceborne lidar, advanced topographic laser altimeter system (ATLAS).[35,36] However, the minimum accuracy of discrete-point lidar determined by the time jitter of the system is 31 mm. In the photon-counting full-waveform lidar, the waveform is the time distribution of photon counts accumulated using the TCSPC technique. A high repetition rate of the laser pulses is used to count enough pulses during a short measurement period. A total of 2000 pulses are counted in 1 ms, as well as ∼300 photon counts accumulating to form the TCSPC curves in Fig. 1(b). The sensitivity of the photon-counting full-waveform lidar is between those of the photon-counting discrete-point lidar and the linear-mode full-waveform lidar.

The full-waveform lidar transmits a narrow-beam laser towards the target, which possibly contains multiple objects. In general, the diffusion reflection power uniformly radiates within a solid angle Ω. Assuming that the solid angle overlaps with the field of view of the receiving telescope, the received echo laser power P_r is given by

$$P_r = \frac{4P_t}{\pi L^2\theta^2}\rho A_s T_s T_a \frac{1}{\Omega L^2}\frac{\pi D^2}{4}, \tag{1}$$

where P_t is the output laser power, θ is the divergence angle of the laser beam, L is the distance, ρ is the reflectivity of the scattering surface, A_s is the scattering area of the objects, D is the diameter of the receiving telescope, T_s and T_a are the optical transmission efficiencies in the receiver and in air, respectively. The received average photon number per pulse is

$$\mu = \frac{P_r}{h\nu f}, \tag{2}$$

where ν is the laser frequency, and f is the repetition rate of the laser pulses. To separate the parameters of the lidar system and the measured target, μ can be described as

$$\mu = \frac{P_t D^2 T_{opt} T_{tran}}{4\pi L^4\theta^2 h\nu f}\sigma, \tag{3}$$

$$\sigma = \frac{4\pi}{\Omega}\rho A_s \propto \mu L^4, \tag{4}$$

where σ is the backscatter cross section, which consists only of the target information, such as surface area, reflectivity and scattering direction. The backscatter cross section can be precisely calculated using Eq. (4). We can also define a relative backscatter cross section σ_r, as μL^4 to compare different backscatter cross sections. The parameter μ is obtained from the Poisson distribution

$$R = 1 - e^{-\mu\eta}, \tag{5}$$

where R is the echo counting rate per pulse, and η is the detection efficiency of the single-photon detector. In the following, we use the parameters of target distance L, peak amplitude A, peak width d, and relative backscatter cross section σ_r, to further analyze the different objects.

To simulate a vertically multilayered structure and to acquire plentiful waveforms, we choose a tree and a building as the trial targets. A photographic picture of the targets is shown in Fig. 2(a). The experiment was conducted at night. The target distance from the

lidar was approximately 250 m. The repetition rate of the laser pulses was 2 MHz, hence the range ambiguity of the system was 75 m. In the experiment, a time delay of 1350 ns was applied in the trigger circuit so that the measurement range was shifted from 202.5 m to 277.5 m. Moreover, the lidar system was installed on a mechanical rotating platform to scan the imagery.

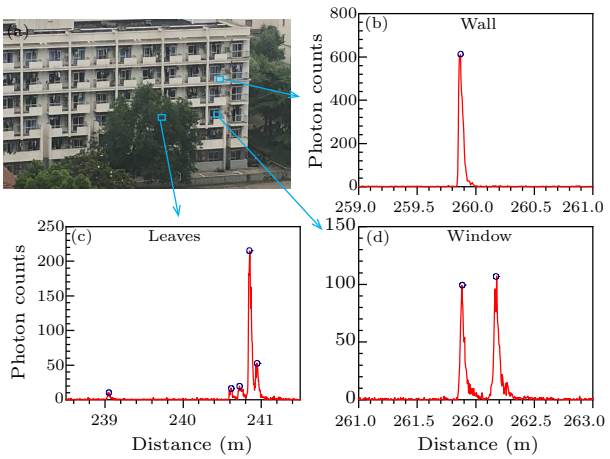

Fig. 2. Three typical echo waveforms from different objects. The pulse peaks were circled in blue. (a) A photographic picture of the target. (b) The waveform of the solid wall with high echo photon counts, which indicates the high albedo of the scattering surface. (c) The waveform of the trees showing uneven peaks, describing the multiple layers of the tree leaves on the vertical axis. (d) The waveform of the windows showing two close and similar peaks.

First, the lidar measures some typical objects to determine characteristic information. The echo waveforms consist of one or more pulse peaks representing various features due to the scattering surface and vertical structure. It is necessary to pick some representative waveforms as a reference. A peek-seeking and counting algorithm routine is then used to analyze the waveforms. The typical photon-counting waveforms are shown in Figs. 2(b)–2(d) with an accumulated time of 10 ms, and the pulse peaks are circled in blue. Using these typical waveforms, we could know roughly the construction of different waveforms. Such typical waveforms identify the basic waveforms of the targets, which models the scatterers for classification purposes. In the following collection of data, the parameter values for L, A, d and σ_{r} of each peak are recorded at the same time.

Second, the lidar scans 180 horizontal points on the target with the interval angle of 0.03° to acquire the profile of the target. The accumulated time at each point is 10 ms, as in our trial above. For each laser footprint, there are multiple echo peaks from the scatters. We establish the vertical distribution of the targets along with the distance. The structures of the leaves and walls are displayed in Fig. 3. It exhibits good penetration of the targets since the walls behind the tree are also recorded by the full waveforms. According to the baseline of the walls, the distance between the tree and walls could be calculated. That also simulates the application of measuring canopy heights in airborne carbon surveying and mapping.

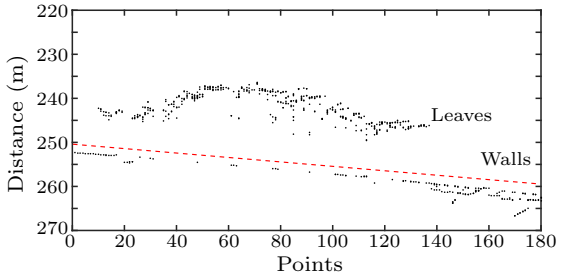

Fig. 3. The profile of the target with 180 points. The wall baseline is marked in red. The intervals between leaves and walls could be used to estimate heights of the trees.

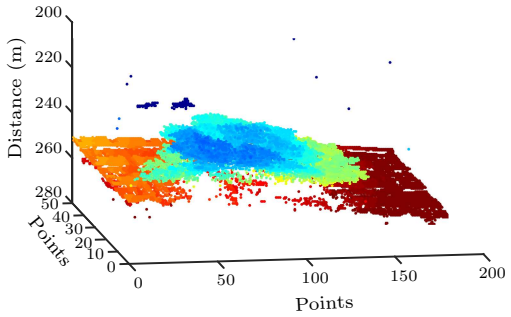

Fig. 4. The 50×180-point cloud image. Different layers are colored to show the depths.

Third, a 50×180-point cloud is acquired by scanning to describe the entire distribution of the tree and walls. The scanning resolution is set at 0.03° per point in the horizontal direction and 0.06° per point in the vertical direction. The accumulated time for each point is still set to 10 ms. Only the distance component is considered in this point-cloud graph. The layers are colored using different colors according to range, as seen in Fig. 4. As in the previous trial, the signals through the leaves could also be detected.

Except for the point cloud, which shows a representation, we use 2D images based on the different components of the waveforms. There are many alternatives for the representation of each waveform since multiple peaks exist in the vertical direction. Here we take the highest peak of the waveform into account to represent the key information. Certainly, the first peak of the waveform could also be drawn to display the canopy features; however, we do not discuss it here. Therefore, the plane pictures of different peak components are illustrated in Fig. 5. From the distance component in Fig. 5(b), we could not differentiate the objects that are located within the same distance, as in the conventional ranging systems. The component of peak amplitude in Fig. 5(c) classifies the objects by intensity, with walls, windows and metal rails having high values. The peak amplitude is responsible for most of the spatial variation of relative

backscatter cross section in Fig. 5(e). However, the backscatter cross section provided an advantage when the decline angle of the scatter surface changed. The peak width in Fig. 5(d) is a significant component to highlight the sloping surface, circled and labeled as A and B, which is especially important when dealing with complex terrain. In addition, the number of peaks shown in Fig. 5(f) is considered in each waveform to indicate the complexity of vertical structures of the objects.

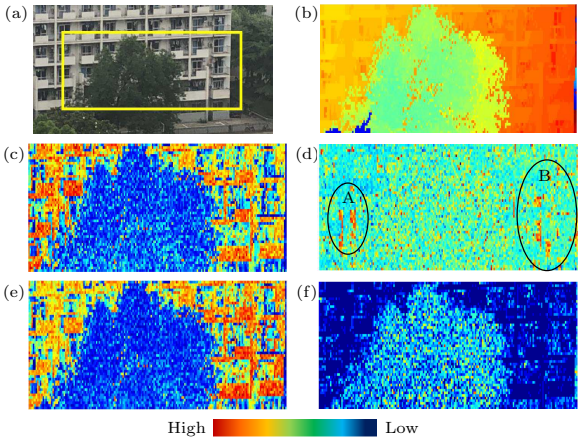

Fig. 5. (a) A photographic picture of the target where the yellow box indicates the scanning area of the lidar system. The intensity pictures classify the targets using different components, such as distance L (b), peak amplitude A (c), peak width d (d), relative backscatter cross section $\sigma_{\rm r}$ (e) and number of peaks (f).

Finally, we show the feasibility of this lidar in the long-range measurement. In the previous experiments, we demonstrate the multiple-repetition-rate laser ranging system to extend the unambiguous measurement range with a high-frequency laser.[37–39] This method of multiple-repetition-rate could be used in the full-waveform lidar system to improve the measurement range. In the verification test, the laser spot of the lidar system covers three boxes with different materials and different distances, which roughly simulates the outdoor targets. Two repetition rates approaching 10 MHz are used to drive the laser diode. The period times are 100 ns and 103 ns, respectively, which support the 1500-m unambiguous measurement. Figure 6(a) shows the target waveforms with the two repetition rates of the laser pulses. Since two waveforms describe the same target, the shapes of the waveforms are almost the same, and the value of the delay time determines the real distance. To figure out the delay time, we shift one of the waveforms (the 103 ns waveform here) to calculate the correlation coefficient in Fig. 6(b). The result shows that the maximum correlation coefficient is 0.969 when the shifting time is 12.0 ns. We derive the distance from all the boxes to be 62.81 m, 63.52 m and 64.01 m, due to the positions of all the peaks in 100 ns waveform at 18.74 ns, 23.44 ns and 26.74 ns, respectively. Although it takes double the amount of time to record two waveforms, these waveforms could be superimposed by shifting the delay time, as shown in Fig. 6(c), to obtain double the counts, counteracting the influence. It stays fairly consistent when analyzing the parameters of each peaks. Furthermore, if we use three or more repetition rates to add to the unambiguous measurement range, then the spaceborne photon-counting full-waveform lidar will be obtainable.

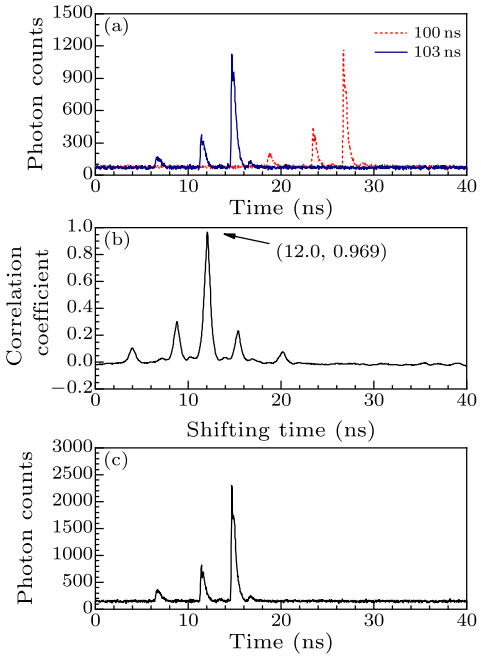

Fig. 6. (a) The waveforms of three boxes with two repetition rates of laser pulses. The period times are 100 ns and 103 ns. (b) Two waveforms have the maximum correlation coefficient when the shifting time is 12.0 ns. (c) Two waveforms are superimposed to obtain double photon counts to offset the acquisition time consumption. The shape of the waveform is maintained.

In conclusion, we have demonstrated the use of a photon-counting lidar applied to full-waveform measurement. A 3D point cloud is acquired to describe the vertical structures of the targets. The parameters of peak position, peak amplitude, peak width and backscatter cross section are used to characterize the surface features of targets for classification. Compared with the linear-mode full-waveform lidar, the photon-counting full-waveform lidar is superior in resolution and accuracy. The unambiguous measurement range of the system could be further improved using the method of combining multiple repetition rates of laser pulses, which will allow airborne or spaceborne full-waveform lidars to perform with high accuracy.

References

[1] Sun S and Salvaggio C 2013 *IEEE J. Sel. Top. Appl. Earth Observ. Remote Sens.* **6** 1440
[2] Jakubiec A and Reinhart C F 2013 *Sol. Energy* **93** 127
[3] Luo S, Wang C, Xi X et al 2014 *Opt. Express* **22** 5106

[4] Schulien J A, Behrenfeld M J, Hair J W et al 2017 *Opt. Express* **25** 13577
[5] Wei G, Shalei S, Bo Z et al 2012 *ISPRS J. Photogramm. Remote Sens.* **69** 1
[6] Hakala T, Suomalainen J, Kaasalainen S et al 2012 *Opt. Express* **20** 7119
[7] Li W, Niu Z, Sun G et al 2016 *Opt. Express* **24** 4771
[8] Bruggisser M, Roncat A, Schaepman M E et al 2017 *Remote Sens. Environ.* **196** 28
[9] Wallace A M, Ye J, Krichel N J et al 2010 *EURASIP J. Adv. Signal Process.* **2010** 896708
[10] Wallace A M, McCarthy A, Nichol C J et al 2013 *IEEE Trans. Geosci. Remote Sens.* **52** 4942
[11] Degnan J 2016 *Remote Sens.* **8** 958
[12] Mallet C and Bretar F 2009 *ISPRS J. Photogramm. Remote Sens.* **64** 1
[13] Zwally H J, Schutz B, Abdalati W et al 2002 *J. Geodynamics* **34** 405
[14] Li H, Chen S, You L et al 2016 *Opt. Express* **24** 3535
[15] Bao Z, Liang Y, Wang Z et al 2014 *Appl. Opt.* **53** 3908
[16] Antolovic I M, Bruschini C and Charbon E 2018 *Opt. Express* **26** 22234
[17] Ren X, Connolly P W R, Halimi A et al 2018 *Opt. Express* **26** 5541
[18] Kirmani A, Venkatraman D, Shin D et al 2014 *Science* **343** 58
[19] O'Toole M, Lindell D B and Wetzstein G 2018 *Nature* **555** 338
[20] Swatantran A, Tang H, Barrett T et al 2016 *Sci. Rep.* **6** 28277
[21] Warburton R E, McCarthy A, Wallace A M et al 2007 *Opt. Lett.* **32** 2266
[22] Maccarone A, McCarthy A, Ren X et al 2015 *Opt. Express* **23** 33911
[23] McCarthy A, Ren X, Frera A D et al 2013 *Opt. Express* **21** 22098
[24] Xia H, Shentu G, Shangguan M et al 2015 *Opt. Lett.* **40** 1579
[25] Ren X, Altmann Y, Tobin R et al 2018 *Opt. Express* **26** 30146
[26] Nie S, Wang C, Xi X et al 2018 *Opt. Express* **26** A520
[27] Buller G and Wallace A 2007 *IEEE J. Sel. Top. Quantum Electron.* **13** 1006
[28] Ren M, Gu X, Liang Y et al 2011 *Opt. Express* **19** 13497
[29] Liang Y, Huang J, Ren M et al 2014 *Opt. Express* **22** 4662
[30] Li Z, Wu E, Pang C et al 2017 *Opt. Express* **25** 10189
[31] McCarthy A, Krichel N J, Gemmell N R et al 2013 *Opt. Express* **21** 8904
[32] Tobin R, Halimi A, McCarthy A et al 2017 *Opt. Eng.* **57** 031303
[33] Steinvall O, Sjöqvist L and Henriksson M 2012 *Proc. SPIE* **8375** 83750C
[34] Henriksson M, Larsson H, Grönwall C et al 2016 *Opt. Eng.* **56** 031204
[35] Harding D, Dabney P, Abshire J et al 2010 *NASA Earth Sci. Techno. Forum* **2010** 22
[36] Markus T, Neumann T, Martino A et al 2017 *Remote Sens. Environ.* **190** 260
[37] Hiskett P A, Parry C S, McCarthy A et al 2008 *Opt. Express* **16** 13685
[38] Krichel N J, McCarthy A, Collins R J et al 2010 *Proc. SPIE* **7681** 768108
[39] Du B, Pang C, Wu D et al 2018 *Sci. Rep.* **8** 4198